nature catalysis

Article

https://doi.org/10.1038/s41929-024-01248-8

Steam methane reforming using a regenerable antenna–reactor plasmonic photocatalyst

Received: 14 August 2023

Accepted: 9 October 2024

Published online: 1 November 2024

Check for updates

Yigao Yuan[1], Jingyi Zhou[2], Aaron Bayles[1], Hossein Robatjazi[1,3], Peter Nordlander[2,4,5] & Naomi J. Halas[1,4,5]

Steam methane reforming (SMR) is the major industrial process for hydrogen production. It currently relies on high-temperature operating conditions and is associated with high carbon intensity. Photocatalytic SMR could provide greener and potentially more efficient H_2 production. Here we demonstrate a plasmonic photocatalytic approach based on a Cu–Rh antenna–reactor photocatalyst for highly reactive, selective and stable SMR due to plasmon-mediated hot carrier contributions. We observe that the photocatalyst is intrinsically stable in photocatalysis but deactivates under thermocatalysis; however, the thermally deactivated catalyst can be regenerated by resonant illumination. The regeneration mechanism is studied in detail and found to be caused by plasmon-induced associative desorption of oxygen and carbon species.

Methane from natural gas, methane hydrate and shale gas is abundant; however, the C–H bond in CH_4 is relatively chemically inert. Numerous studies have demonstrated CH_4 activation and its conversion into value-added chemicals, including hydrogen[1,2], methanol[3,4], ethane[5,6] and aromatic molecules[1,7,8]. Among these processes, steam methane reforming (SMR; $CH_4 + H_2O \rightleftharpoons 3H_2 + CO$; change in enthalpy ($\Delta H$) = 206 kJ mol^{-1}) is particularly important, accounting for half of the current global hydrogen production[9,10]. SMR produces syngas (H_2 and CO)—a major feedstock for industrial chemical reactions such as Fischer–Tropsch synthesis[11–13]. Despite SMR having been utilized since the 1930s[14], traditional thermal processes face major obstacles, including the requirement for high temperature, coking and extreme carbon intensity. Photocatalytic SMR has the potential to circumvent high temperatures by utilizing light to reduce the activation energy[15–17]. However, its application has hitherto been confined to ultraviolet light illumination[18–21] or necessitated additional external heating[22,23]. Detailed summaries of recent progress on photocatalytic SMR are provided in table 1 of ref. 16 and table 2 of ref. 17.

Plasmonic photocatalysis[24–27], utilizing hot carriers from surface plasmon decay in metal nanoparticles, could overcome the limitations associated with the above listed attempts at photocatalytic SMR[18–23]. Plasmonic photocatalysis has been demonstrated with various systems, including Au[28–30], Ag[31,32], Cu[33] and Al nanostructures[34]. Combining plasmonic materials with traditionally known catalytically active but optically inferior transition metals to form antenna–reactor (AR) complexes has further expanded the scope of heterogeneous photocatalysis, showing enhancement in the reactivity, selectivity and stability of various chemical reactions[35–37]. ARs have been demonstrated for a number of important chemical processes, such as H_2 production from ammonia decomposition[38,39], syngas (H_2 and CO) production from methane dry reforming[40] and other reactions[41,42]. In this Article, we demonstrate that by combining plasmonic Cu antennas with catalytically active Rh in the form of a Cu–Rh surface alloy, AR photocatalysts can provide a path to efficient and selective photocatalytic SMR. The photocatalytic SMR is primarily driven by plasmon-mediated hot carriers, which reduces the apparent energy barrier and contributes to catalytic stability. Without hot carriers, thermocatalysis deactivates the catalyst due to oxidation and coking. The thermally deactivated catalyst can be regenerated in photocatalysis, recovering the reactivity and selectivity under illumination conditions.

---

[1]Department of Chemistry, Rice University, Houston, TX, USA. [2]Department of Materials Science and NanoEngineering, Rice University, Houston, TX, USA. [3]Syzygy Plasmonics, Houston, TX, USA. [4]Department of Electrical and Computer Engineering, Rice University, Houston, TX, USA. [5]Department of Physics and Astronomy, Rice University, Houston, TX, USA. e-mail: nordland@rice.edu; halas@rice.edu

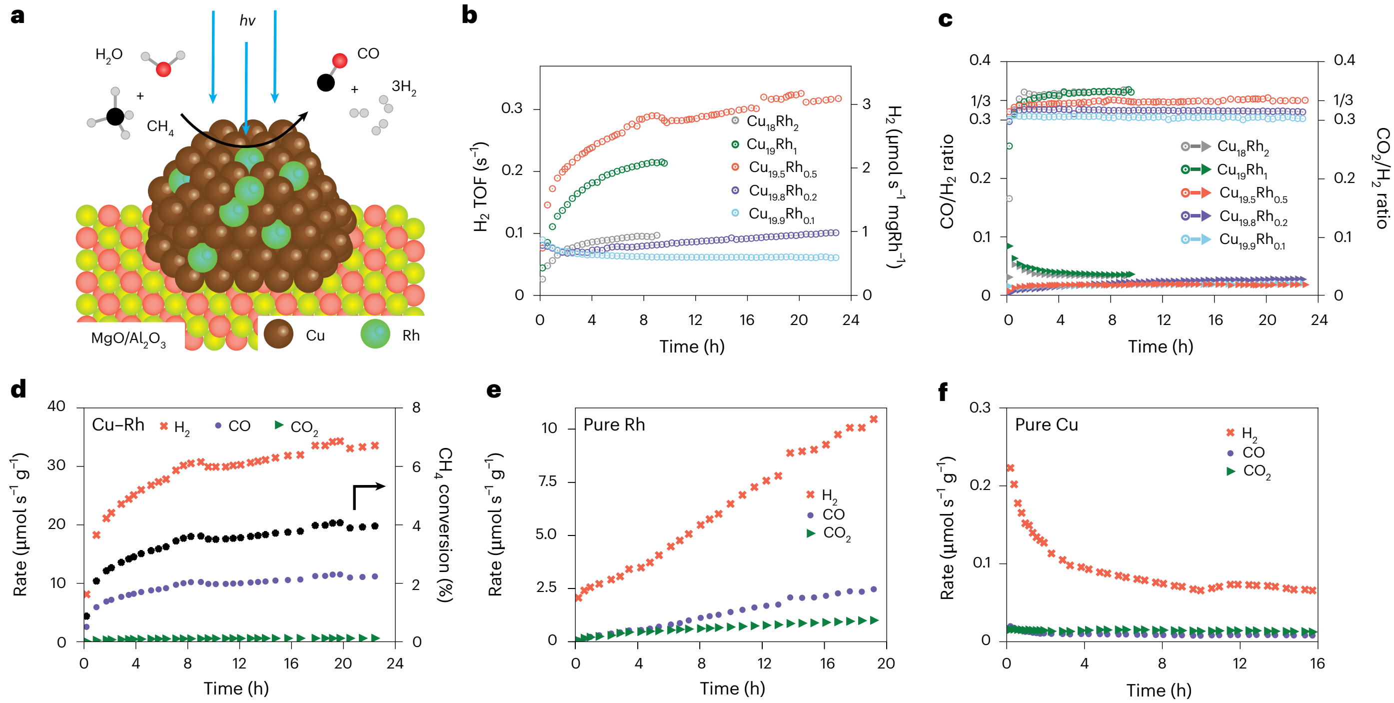

Fig. 1 | Photocatalytic SMR. a, Schematic of the photocatalytic SMR reaction on the Cu–Rh AR catalyst on a metal oxide support. **b**, Reactivity and stability profile of $Cu_{20-x}Rh_x$ photocatalysts. **c**, Selectivity profiles of CO and CO_2 for the same samples shown in **b**, plotted as the ratios of CO/H_2 (circles) and CO_2/H_2 (triangles). **d**–**f**, Reactivity, selectivity and stability profiles of the Cu–Rh AR (**d**) compared with pure Rh (**e**) and pure Cu (**f**) catalyst. The reaction conditions were as follows: 0.5 W white light illumination, 3% CH_4 and 3% H_2O with balancing He (at a total flow rate of 20 sccm) under ambient pressure, 1.5 mg photocatalyst and no external heating.

Results

Photocatalytic SMR

Here we show that reactive, selective, and stable photocatalytic SMR can be achieved using a Cu–Rh AR photocatalyst (Fig. 1a). Cu was adopted as the antenna because of its relatively high abundance and efficient generation of hot carriers[43]. Previous thermocatalysis studies indicated that Ni-, Ru-, Pt- and Rh-based catalysts are most commonly used for SMR[14,44] and alloys such as Ni–Au[45] and Cu–Pt[46] show coking resistance by weakening the binding strength of carbon species at the expense of higher C–H activation barriers. Our initial photocatalysis investigations using Cu–Ni ARs with various Ni loadings (0.2–10.0 at%) showed low reactivity, poor selectivity and persistent coking (Supplementary Fig. 1). The Cu–Pt ARs, despite having higher reactivity than Cu–Ni ARs, were not selective towards either CO or CO_2 (Supplementary Fig. 2b,e). Cu–Pt ARs also suffered from coking, as indicated by Raman spectroscopy after the reaction (Supplementary Fig. 2c,f). The Cu–Ru ARs demonstrated no coking, but the product selectivity was low (Supplementary Fig. 2h,k). By contrast, the Cu–Rh ARs (Fig. 1) showed the highest reactivity, selectivity and stability. A similar trend has been noted in other systems; for instance, first principles calculations have indicated that Rh and Ru exhibit higher reactivity compared with Pt and Ni species[44]. Likewise, a Rh-doped Cu single-atom catalyst has demonstrated a lower C–H activation energy compared with Pt-, Pd- and Ni-doped Cu alloys[47]. The Cu–Rh AR photocatalysts at various loadings were prepared using a robust co-precipitation method[48,49] (Methods), in which Rh reactors were adjacent to or alloyed with Cu nanoparticles (Supplementary Fig. 3c,f). The resulting Cu–Rh AR nanoparticles were semispherical with an average size of 16 nm (Supplementary Fig. 3g) and were supported on MgO/Al_2O_3 powders (Supplementary Fig. 4).

The Cu–Rh ARs are denoted by $Cu_{20-x}Rh_x$, where x is the atomic loading of Rh. We tested $Cu_{20-x}Rh_x$ with $x = 0.1, 0.2, 0.5, 1.0$ and 2.0 and found that $Cu_{19.5}Rh_{0.5}$ achieved the best reactivity (Fig. 1b), stability and selectivity (Fig. 1c) under white light laser illumination at 3% CH_4 and 3% H_2O feeding in a fixed bed continuous flow reactor (Methods and Supplementary Fig. 5b). The $Cu_{19.5}Rh_{0.5}$ photocatalyst showed the highest H_2 turnover frequency (TOF), up to 0.308 s^{-1} (0.308 moles of H_2 per mole of Rh per second, or 2.99 μmol H_2 per mg Rh per second). By definition, the H_2 TOF is the same as the site–time yield of H_2 defined previously[50]. When normalizing the absolute H_2 rate to the volume of the catalyst bed (Supplementary Fig. 5c), a space–time yield of 15.6 μmol cm^{-3} s^{-1} was achieved. Compared with the benchmark value of 1 μmol cm^{-3} s^{-1} for large catalytic processes[17,50], our value of 15.6 μmol cm^{-3} s^{-1} clearly shows the potential for plasmon-enhanced photocatalytic SMR technology in sustainable industrial H_2 production. Photocatalytic SMR could be further scaled up by at least three orders of magnitude using the previously reported gram-scale photoreactor[38]. The selectivity was quantified using the molar ratio between CO and H_2, where the ideal value of 1/3 is based on the stoichiometry of the SMR reaction. However, side reactions known for SMR, such as the Boudouard reaction ($2CO \rightleftharpoons CO_2 + C$; $\Delta H = -172$ kJ mol^{-1}), methane pyrolysis ($CH_4 \rightleftharpoons 2H_2 + C$; $\Delta H = 75$ kJ mol^{-1}) and the water–gas shift reaction ($CO + H_2O \rightleftharpoons CO_2 + H_2$; $\Delta H = -41$ kJ mol^{-1}) could decrease the CO/H_2 value. In contrast, possible side reactions associated with catalyst activation, such as the reduction of Cu and Rh on the stream, would consume the produced H_2, resulting in CO/H_2 ratios exceeding 1/3. Figure 1c shows preferential selectivity towards CO on all Cu–Rh AR samples. $Cu_{19.5}Rh_{0.5}$ showed a CO/H_2 ratio at the ideal stoichiometric value. $Cu_{19}Rh_1$ and $Cu_{18}Rh_2$ catalysts showed slight deviation from the ideal CO/H_2 ratio (Fig. 1c, green curve). This deviation could be associated with side reactions, as well as the standard uncertainty in gas delivery systems, sampling and quantification from gas chromatography (equation (11) in Methods). No other hydrocarbon products were observed in the gas chromatography spectrum (Methods and Supplementary Fig. 6). As shown, the reactivity and selectivity of Cu–Rh ARs depends on Rh loadings, which should be neither too low nor too high to maximize both reactivity and selectivity. The loading dependence is possibly related to

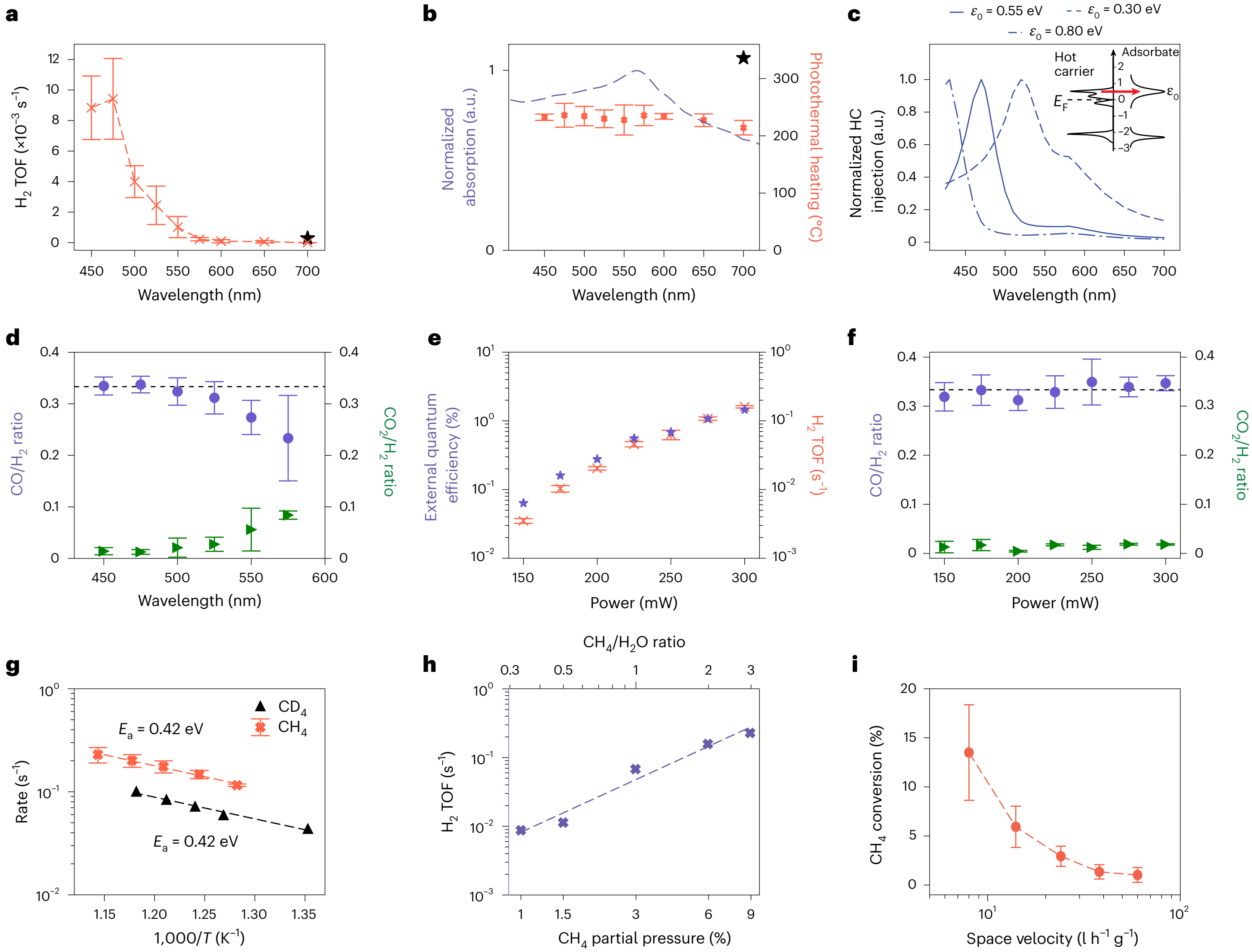

Fig. 2 | Study of the mechanism of photocatalytic SMR. a, Wavelength-dependent H_2 TOF under 0.1 W illumination. The black star represents H_2 TOF at an illumination of 0.2 W and a wavelength of 700 nm. **b**, Normalized optical absorption (left *y* axis; blue) and photothermal heating (right *y* axis; red) at various wavelengths under 0.1 W illumination. The black star represents photothermal heating at an illumination of 0.2 W and a wavelength of 700 nm. **c**, Normalized hot carrier (HC) injection rates at various wavelengths when the antibonding orbital (ε_0) was centred at 0.30, 0.55 or 0.80 eV. Inset, hot carrier injection model. E_F is the Fermi energy. **d**, Selectivity profiles (CO/H_2 (blue) and CO_2/H_2 (green) ratios) of the experiments shown in **a**. The dashed lines in **d** and **f** are visual guides representing the ideal ratio of 1/3. **e**, Power-dependent H_2 production rate (right *y* axis; red) and external quantum efficiency (left *y* axis; blue). **f**, Selectivity profiles (CO/H_2 (blue) and CO_2/H_2 (green) ratios) of the experiments shown in **e**. **g**, Apparent activation barrier measurements for CH_4 (red) and its isotopologue CD_4 (black). Maximum surface temperatures were used. **h**, CH_4 reaction order measurement under 0.2 W white light. The dashed line represents the linear regression fitting. **i**, CH_4 conversion at various reactant CH_4 feeding rates. The error bars in **a**, **b**, **d**–**g** and **i** represent the standard deviation of three independent measurements. The reaction conditions were as follows: 3% CH_4 and 3% H_2O with balancing He (at a total flow rate of 20 sccm) under ambient pressure, 1.5 mg photocatalyst and no external heating except for **g** (Methods).

the coordination environment for Rh, which is similar to that of Ru in Cu–Ru[40]. Initial increasing of the Rh loading up to 0.5 mol% increased the total number of reaction sites, whereas additional Rh loading (2%) resulted in the formation of Rh clusters and nanoparticles with a lower Rh dispersion. Thus, the TOF of $Cu_{18}Rh_2$ is lower than that of $Cu_{19.5}Rh_{0.5}$ because the TOF is normalized to each Rh.

Synergistic effects between the Cu antenna and Rh reactor were observed (Fig. 1d–f). The H_2 production rate of the Cu–Rh AR was improved compared with either Cu or Rh. (Fig. 1d). Pure Cu and Rh catalysts showed substantially lower selectivity for either CO or CO_2 compared with the selective CO formation and minimal CO_2 production on the Cu–Rh AR (Fig. 1e,f). These results indicate that both Cu and Rh are essential for photocatalytic SMR and a single catalyst component would not work as effectively. This is consistent with Rh loading dependence (Fig. 1b), where pure Cu and pure Rh represent the two extreme cases. In these cases, reaction intermediates (C species) would bind to the catalyst surface without specificity. However, in the case of $Cu_{19.5}Rh_{0.5}$, C species will bind to Rh instead of Cu because of its higher binding affinity[44], yielding stable and selective CO desorption.

Study of the mechanism of photocatalytic SMR

Our measured wavelength-dependent reactivity and selectivity indicate that photocatalytic SMR is primarily driven by plasmon-mediated hot carriers (Fig. 2a–d). The wavelength dependence was studied by monitoring product formation while varying the excitation wavelength at a constant illumination power of 0.1 W. The corresponding power density (8.5 W cm^{-2}), beam profile and repetition rate (78 MHz) were identical within experimental error, allowing us to compare the measured reaction rates as a function of illumination wavelength. A strong wavelength-dependent reactivity trend was observed with

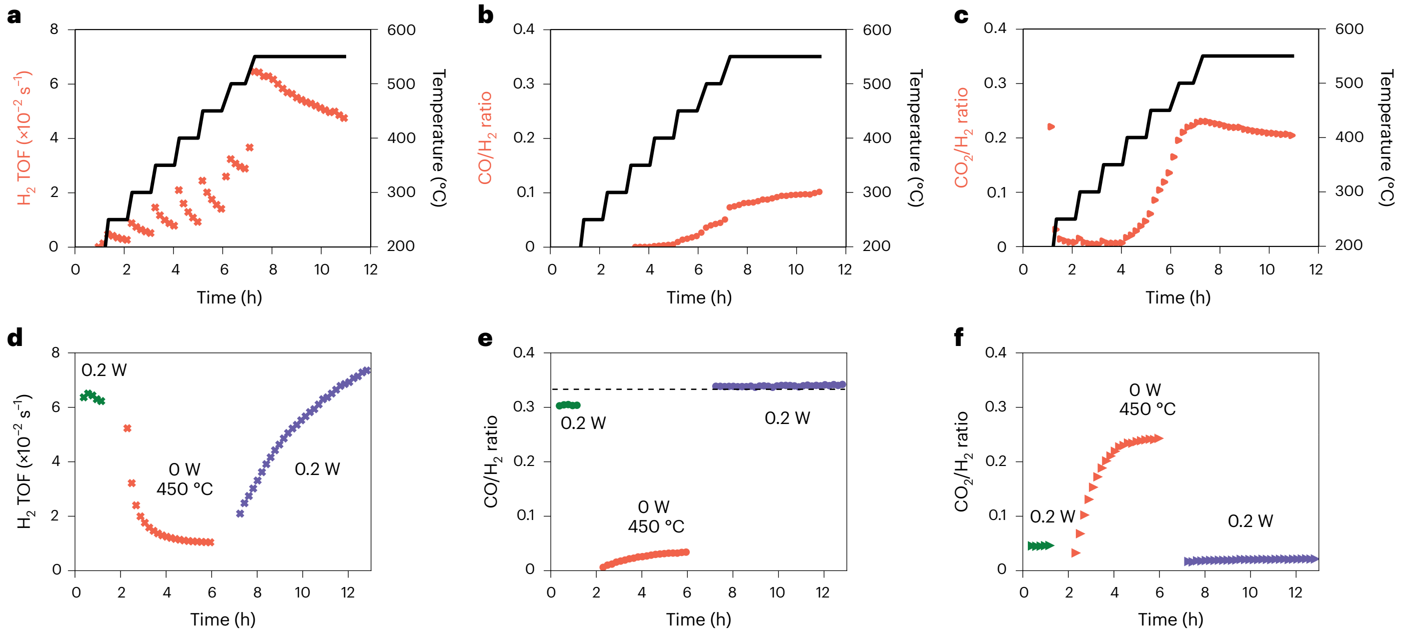

Fig. 3 | Thermocatalytic deactivation and photocatalytic regeneration. **a**–**c**, Results of thermocatalysis studies, showing H_2 TOF (**a**), the CO/H_2 ratio (**b**) and the CO_2/H_2 ratio (**c**) over time, along with the corresponding temperatures. **d**–**f**, Results of the regeneration studies in which photocatalysis (green), thermocatalysis (red) and photocatalysis (blue) were performed in sequential order. Values of H_2 TOF (**d**), the CO/H_2 ratio (**e**) and the CO_2/H_2 ratio (**f**) are shown. The dashed line in **e** represents the ideal stoichiometric CO/H_2 ratio of 1/3. The reaction conditions were as follows: 3% CH_4 and 3% H_2O with balancing He (at a total flow rate of 20 sccm) and 1.5 mg photocatalyst under ambient pressure.

peak reactivity occurring at ~475 nm illumination (Fig. 2a). By contrast, the optical absorption spectrum peaked at a distinctly different wavelength of ~570 nm (Fig. 2b and Supplementary Fig. 5a), whereas the Cu interband transition had an onset at a wavelength of ~600 nm[51]. Photothermal heating during the experiment was monitored using an infrared camera (Methods) and represented by the measured maximum surface temperature (Fig. 2b and Supplementary Fig. 5d), as described previously[52,53]. The wavelength-dependent reactivity did not follow the trend of photothermal heating, indicating that the reaction was not dominated by photothermal heating. Photothermal contributions were also found to be negligible based on a simple control experiment in which the SMR reaction was run at an illumination wavelength of 700 nm and a laser power of 0.2 W. The surface temperature increased by ~100 °C (black star in Fig. 2b), without an increase in reactivity (black star in Fig. 2a). Altogether, these results suggest that hot carriers play a major role in photocatalytic SMR.

The wavelength-dependent reactivity was simulated using a hot carrier injection model[38], which relates the hot carrier distribution to the antibonding orbital of the adsorbate (Fig. 2c, inset). The hot carrier distribution was calculated from the electronic structure of Cu and the excitation wavelengths (Supplementary Fig. 7a). The antibonding orbital of the adsorbate was modelled as a Lorentzian function (Methods) with a centre energy 0.55 eV above the Fermi level (Fig. 2c). A calculation of the wavelength-dependent hole injection rate into bonding orbitals (Supplementary Fig. 7b,c) did not correlate with the observed reactivities. Cumulatively, these observations are consistent with a hot electron mechanism resulting in the formation of a transient negative ion state[54,55]. The peak reactivity was sensitive to the energy of the antibonding orbital: only hot carriers with sufficient energy were able to access the available adsorbate–metal states to drive the chemistry. We also observed wavelength-dependent selectivity (Fig. 2d), where CO production followed the trend of hot carrier injection, with the CO/H_2 ratio achieving the ideal stoichiometric value of 1/3 at ~475 nm. Fine tuning of the wavelength enabled control of the CO or CO_2 yields, highlighting the potential for optical control of chemical selectivity in plasmon-driven catalysis. The external quantum efficiency, defined as the number of H_2 molecules produced divided by the number of incident photons, showed a superlinear relationship with the increase in illumination power (Fig. 2e). By doubling the illumination intensity from 150 to300 mW, the reactivity and efficiency were enhanced by more than one order of magnitude (Fig. 2e). This strongly nonlinear response provides another path for further optimization of the reaction. The selectivity was less sensitive to power, where CO was the main product, with a CO/H_2 ratio close to the ideal stoichiometric value for all powers (Fig. 2f).

We assessed the influence of light on the apparent activation barrier (E_a) of the reaction under constant illumination and varying external heating (Fig. 2g and Supplementary Fig. 8a). At 300 mW and 467 nm illumination, the measured E_a of 0.42 ± 0.044 eV (40.5 ± 4.2 kJ mol^{-1}) was lower than those previously reported in thermocatalysis and photocatalysis studies (51.5 kJ mol^{-1})[22]. We also performed thermocatalytic SMR under varied applied external heating, but the calculation of E_a was not attempted due to instability in the thermocatalysis (Fig. 3a). Further characterization (Fig. 4) revealed carbon deposition and oxidation post-thermocatalysis, indicating that deactivation resulted from the failure to desorb surface carbon and oxygen species. This observation aligns with previous reports suggesting that the associative desorption of CO is the rate-determining step (RDS) of SMR in thermocatalysis at low temperatures on Rh[44]. To gain further insights into the influence of light on the RDS of the photocatalysis reaction, an isotope experiment was performed using fully deuterated methane (CD_4). The reactivity slowed down when CH_4 was substituted with CD_4, with a measured kinetic isotope effect of $k_H/k_D = 1.9$ (Fig. 2g). However, as the difference in zero-point energy between CD_4 and CH_4 was negligible (within the fitting error of the Arrhenius plot), the resulting E_a remained similar to that of the CH_4 case. Nevertheless, the positive kinetic isotope effect (Fig. 2g) suggested that CH_4 dissociative adsorption is the RDS in photocatalysis SMR on the Cu–Rh AR catalyst. The RDS shifted from CO associative desorption in thermocatalysis to CH_4 dissociative adsorption in photocatalysis. This phenomenon aligns with observations in previous studies[38,39], where plasmonic hot carriers facilitated the associative desorption of the product so that the RDS shifted to

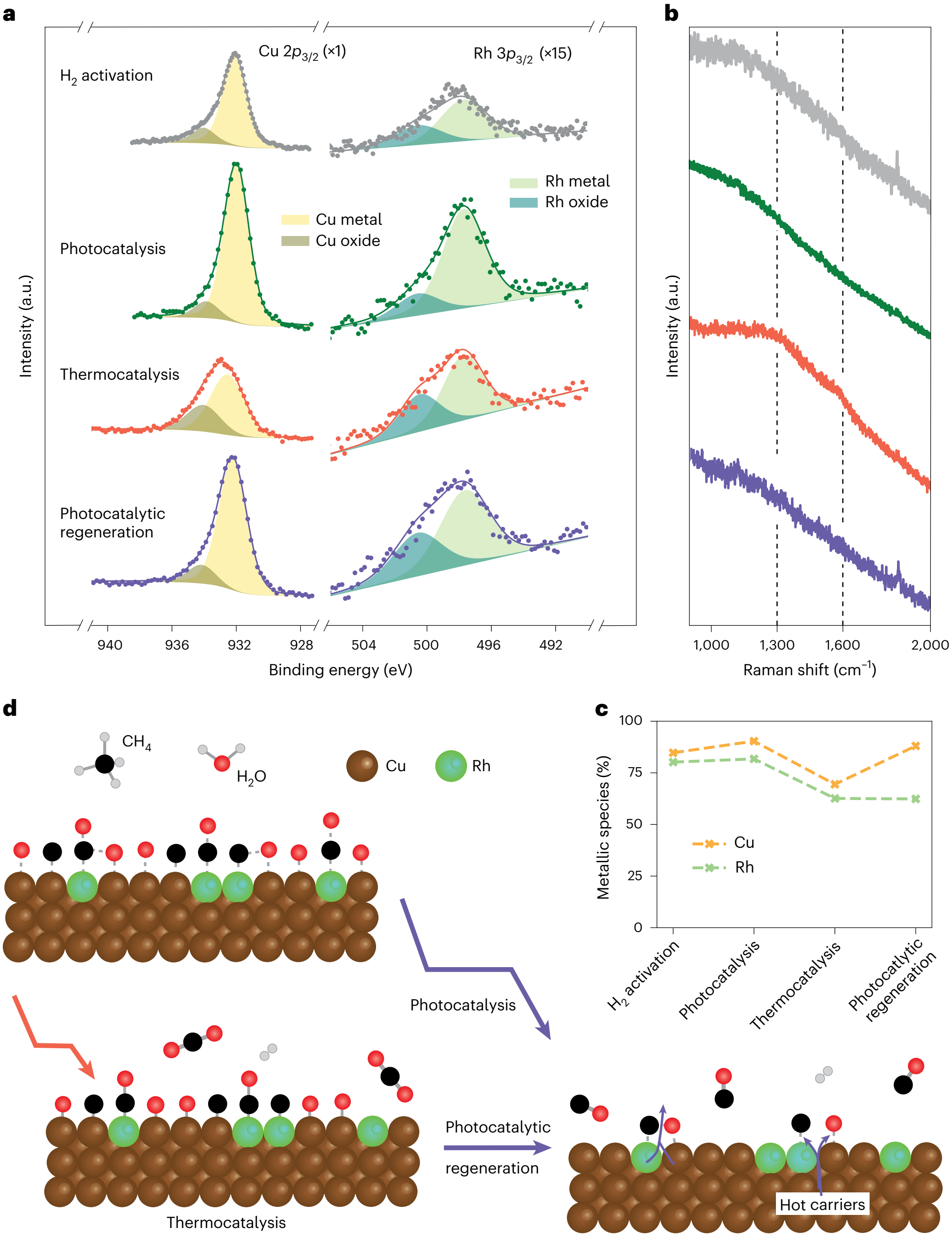

Fig. 4 | Study of the mechanism of photocatalytic regeneration. **a**, XPS survey of the Cu–Rh AR after initial H_2 activation, photocatalysis, thermocatalysis and photocatalytic regeneration. The label ×15 indicates that the signal was amplified 15-fold for visualization purposes. The Cu 2p and Rh 3p spectra were deconvoluted to determine the metallic and oxide species fractions. Lines of best fit have been drawn through the raw data points. **b**, Raman spectroscopy of the Cu–Rh AR following the same treatments as in **a**. The two dashed lines are visual guides for the defect and graphite bands of carbon. **c**, Metallic species as a percentage of the total oxide and metallic species of Cu and Rh, as shown in **a**. **d**, Schematic of the proposed mechanism of oxidation and coking in thermocatalytic deactivation and hot carrier-assisted photocatalytic regeneration. H atoms on the catalyst surface were omitted due to their high mobility and facile desorption.

dissociative adsorption of the reactant. In fact, hot carriers are known to facilitate associative desorption through the desorption induced by the electron transition mechanism[56,57]. The E_a is also affected by illumination power and wavelength. The decrease in E_a correlated with increasing the illumination power (Supplementary Fig. 8b). Moreover, the blue wavelength exhibited lower E_a and higher reactivity compared with the red wavelength, in agreement with the wavelength-dependent results shown in Fig. 2a.

Partial pressure of the reactants is another factor that influences the kinetics of chemical reactions. The reactivity increased by more than one order of magnitude when increasing the CH_4 partial pressure (1–9%), with a reaction order of ~1.6 at 0.2 W (Fig. 2h and Supplementary Fig. 8c). To gain more insights into the role of light in modifying the elementary reaction steps, we performed microkinetic analysis assuming either associative desorption of CO or dissociative adsorption of CH_4 as the RDS. Our analysis (Supplementary Note 1) suggested CH_4

reaction orders of 0 and 1 for the two above scenarios, respectively, with the latter being closer to our measured reaction order of 1.6 for CH_4 in photocatalysis. This analysis further supports a contribution of hot carriers to the energetics of the elementary steps, shifting the RDS from CO associative desorption in thermocatalysis to CH_4 dissociative adsorption in photocatalysis, thus promoting stability and selectivity. We also measured the CH_4 conversion rates as a function of space velocity (Fig. 2i), showing a decrease in the conversation rate from 14 to 1% with an increase in the space velocity from 8 to 60 l h−1 g_{cat}^{-1}.

Thermocatalytic deactivation and photocatalytic regeneration

Unlike photocatalysis, thermocatalytic SMR on the same Cu–Rh ARs showed unstable reactivity with a fast decay rate (Fig. 3a) and low selectivity, producing both CO (Fig. 3b) and CO_2 (Fig. 3c) at temperatures ranging from 250 to 550 °C. Following the deactivation in thermocatalysis, we found that illumination of the photocatalyst without external heating under the same gas environment (3% CH_4 and 3% H_2O with balancing He) could lead to its complete regeneration. The photocatalytic activity and product selectivity were restored, as shown in Fig. 3d–f. In the initial photocatalysis phase, stability was maintained under 0.2 W white light illumination, with CO being the predominant product (green data points in Fig. 3d–f). Subsequently, thermocatalysis was conducted at 450 °C, resulting in a substantial loss of reactivity and a shift towards CO_2 as the dominant product (red data points in Fig. 3d–f). Following thermocatalysis, a recovery in reactivity and selectivity was observed upon returning to the photocatalysis conditions (blue data points in Fig. 3d–f). Catalyst regeneration under optical illumination was repeatedly observed under various conditions (Supplementary Fig. 9). This suggests that hot carriers in photocatalysis not only preserve catalyst performance but also have the capability to restore photocatalyst performance after thermal degradation caused by running the reaction under dark conditions.

Study of the mechanism of photocatalytic regeneration

We studied the catalyst deactivation and regeneration mechanisms in greater detail by investigating the oxidation states and relative abundance of elements. Ex situ X-ray photoelectron spectroscopy (XPS) and Raman spectroscopy studies were performed following initial H_2 activation (the catalyst reduction step), photocatalysis, thermocatalysis and the subsequent photocatalytic regeneration step (Fig. 4a–c). Based on the relative ratio of the metallic copper to its oxide species, illumination further reduced the initially H_2-activated catalyst (the reduction step in the reaction chamber before photocatalysis), consistent with the gradual increase in the photocatalytic H_2 production rate as a function of time shown in Fig. 1b. Thermocatalysis led to substantial catalyst oxidation (Fig. 4a,c), which was associated with the reactivity loss observed above (Fig. 3a). Plasmonic metals such as Ag, Au and Cu are known to form oxides under thermal SMR reaction conditions[44], which would damp the plasmon and reduce its light-harvesting ability. However, subsequent illumination under the reaction conditions (without any external heating) resulted in a notable increase in the metallic Cu/oxide peak ratio (Fig. 4a,c), consistent with the observed gradual recovery in the catalyst activity (Fig. 3d). Rh species remained partially oxidized and partially metallic (Fig. 4a,c), which is likely to represent the active phase of Rh in SMR[20]. Raman spectroscopy (Fig. 4b and Supplementary Fig. 10b) analysis further revealed the formation of amorphous carbon only in thermocatalysis, indicating coking of the catalyst surface. These observations further indicated the contribution of plasmon-mediated hot carriers in efficient and stable photocatalytic SMR. Hot carriers in photocatalysis can facilitate the associative desorption of CO, yielding stoichiometric CO production while simultaneously suppressing CO_2 production from the water–gas shift reaction. Phonons excited in thermocatalysis cannot desorb CO efficiently, resulting in poor selectivity and poor stability. However, the thermally deactivated Cu–Rh AR can be regenerated by hot carriers (Fig. 4d).

Conclusions

In conclusion, we observed that a Cu–Rh AR photocatalyst is reactive, selective and stable for photocatalytic SMR once optimized for Rh loadings and for the wavelength dependence of its photoreactivity. We observed a fast deactivation of the photocatalyst run under thermal, dark conditions, which could be fully regenerated by returning to photocatalytic SMR. By following the detailed elemental evolution of the catalyst through thermal deactivation and photocatalytic regeneration, we observed that hot carrier-related processes promote the associative desorption of C and O intermediates and assist the return of oxidized photocatalyst to their less oxidized states, consistent with a reliable and practical return to photocatalytic activity.

The process of hot carrier-driven desorption resulting in the restoration of photocatalyst activity has an extremely important implication. It may extend catalyst lifetimes and enable the regeneration of deactivated catalysts in general.

Methods

Synthesis of Cu–Rh AR

The synthesis of $Cu_{19.5}Rh_{0.5}$ (19.5 at% Cu and 0.5 at% Rh) was initiated by mixing 2,925 µl of a 1.0 M $Cu(NO_3)_2$ (61194; Sigma–Aldrich) precursor solution (120.8 g $Cu(NO_3)_2{\cdot}3H_2O$ dissolved in 500 ml deionized water from a Milli-Q Advantage A10 system), 1263 µl 0.0594 M $RhCl_3$ precursor solution (156.2 mg $RhCl_3{\cdot}xH_2O$ (520772; Sigma–Aldrich) dissolved in 10 ml deionized water, assuming $x = 3$), 9.0 ml 1.0 M $Mg(NO_3)_2$ (63084; Sigma–Aldrich) and 3.0 ml 1.0 M $Al(NO_3)_3$ (237973; Sigma–Aldrich) and then adding the mixture drop wise into a 150 ml flask while maintaining a pH of 8 by adding 1.2 M Na_2CO_3 (223530; Sigma–Aldrich) as needed. For $Cu_{20-x}Rh_x$ samples with different loadings, the amounts of Cu and Rh precursor solutions were varied accordingly. The co-precipitation reaction was held at 80 °C for 24 h, then washed with Milli-Q water and centrifuged at 1,000*g* five times. Subsequent treatment involved baking in an oven at 120 °C overnight, then grinding and filtering through a 230–400 mesh. The sample was annealed at 600 °C under a constant flow of 50 standard cubic centimetres per minute (sccm) He (Airgas; ultrahigh purity; 99.999%). Then, the sample was reduced at 400 °C under a constant flow of 20 sccm H_2 (Airgas; research purity; 99.9999%). Using the prescribed preparation method, the active samples were Cu–Rh alloy nanoparticles supported on MgO and Al_2O_3.

Cu nanoparticles supported on MgO–Al_2O_3 (20 at% Cu). The preparation of Cu adopted the same method except that the reaction solution contained 3.0 ml 1.0 M $Cu(NO_3)_2$, 9.0 ml 1.0 M $Mg(NO_3)_2$ and 3.0 ml 1.0 M $Al(NO_3)_3$.

Rh nanoparticles supported on MgO–Al_2O_3 (0.5 at% Rh). The preparation of Rh adopted the same method except that the reaction solution contained 1,015 µl 0.0594 M $RhCl_3$, 9.0 ml 1.0 M $Mg(NO_3)_2$ and 3.0 ml 1.0 M $Al(NO_3)_3$. Note that 1,015 µl Rh precursor solution was used instead of 1,263 µl so that the final Rh atomic concentration was 0.5 at%.

Characterization of Cu–Rh ARs

The structure of the Cu–Rh ARs was examined by high-angle annular dark-field scanning transmission electron microscopy, which was performed using an FEI Titan Themis scanning transmission electron microscope equipped with both spherical and chromatic aberration correctors. Samples were reduced before being suspended in isopropanol and then drop cast onto a Ni-lacey carbon transmission electron microscopy grid. The overall structure of the Cu–Rh catalysts was similar to those previously reported for Cu–Ru[39,40]. The active alloy nanoparticles were spherical (Supplementary Fig. 3a,d) with an average diameter of 16 nm for Cu (Supplementary Fig. 3g). Based on energy-dispersive X-ray spectroscopy mapping (Supplementary Fig. 3b,e), Cu tended to form nanospheres, whereas Rh was distributed across the surface, meaning that Rh can be alloyed with Cu, but some free Rh species (probably in the form of sub-nanometre clusters or single atoms; Supplementary Fig. 3c,f) may also exist on the oxide support. Powder X-ray diffraction spectra were measured on a Rigaku D/MAX Ultima II instrument using Cu Kα radiation. Spectra were collected from 30–100° at a speed of 2° min^{-1}. Samples were reduced before being quickly transferred onto the sample holder. Three peaks matching literature values of MgO and no peaks matching Al_2O_3 (Supplementary Fig. 4) were observed, indicating the amorphous nature of Al_2O_3. Cu–Rh had five peaks matching Cu and no peak corresponding to Rh because of the relatively low loading of Rh (Supplementary Fig. 4). Diffuse reflectance was measured using an Agilent Cary 5000 UV-Vis-NIR spectrometer. A Praying Mantis Diffuse Reflectance Accessory (DRP-VA; Harrick Scientific Products) was attached to the spectrometer to convert the light configuration from transmission mode to diffuse reflection mode. After catalyst pre-treatment, the sample was quickly transferred to the Praying Mantis accessory. The spectrum was collected from 400–800 nm with a scan rate of 600 nm min^{-1}. MgO powder (342793; Sigma–Aldrich) was used as a white reference for collection of the background spectrum. Reflectance data were collected using the spectrometer and then converted to absorption values (Fig. 2b) using the Kubelka–Munk diffuse reflectance formula. Raman spectra (Supplementary Figs. 1, 2 and 10) were collected using a Renishaw Raman microscope with a 785 nm excitation wavelength and 5 mW of power. Samples were sealed in the reaction cell, which had an optical window allowing for Raman detection. XPS was performed on a PHI Quantera X-ray photoelectron spectrometer under ultrahigh vacuum conditions with a step size of 0.2 eV and a pass energy of 55 eV. Cu–Rh AR samples were prepared and treated under the corresponding conditions in the Harrick reaction cell and quickly transferred for XPS. All XPS spectra were calibrated by C1s of 284.8 eV.

SMR reaction

Photocatalysis was performed in flow mode under ambient pressure and room temperature. Catalyst (1.5 mg) was loaded in the Harrick reaction chamber, which allowed for laser illumination through a CaF_2 optical window. A supercontinuum white light laser (WL-SC-400-8; Fianium; 400–900 nm; 4 ps; 80 MHz) was used as the illumination source in all of the experiments. The radiant flux (or simply the optical power) was tuned using a neutral-density filter (NDC-100C-2M; Thorlabs) and measured using a thermal power sensor (S401C; Thorlabs). The reactant gas CH_4 (Airgas; ultrahigh purity; 99.999%) and preparation gases were fed into the reaction chamber through gas mass flow controllers (MFCs; Alicat Scientific). The effluent gas was analysed by gas chromatography (GC-2014; Shimadzu). CH_4 was separated using an Rt-Q-BOND capillary column (Restek; 0.53 mm internal diameter; 20 μm film thickness; 30 m capillary column length; 10 °C min^{-1} ramping to 150 °C) and detected using a flame ionization detector. H_2, CO and CO_2 were separated using a ShinCarbon packed column (Restek; 60/80 mesh particle size; 1.59 mm outer diameter; 2 m capillary column length; 100 °C) and detected using a pulsed-discharge helium ionization detector. Alternatively, quadrupole mass spectrometry (QIC-20; Hiden Analytical) could be used to quantify the products. In a typical photocatalysis experiment, CH_4 (0.60 sccm) and balancing He were mixed and flowed through a water bubbler (7533-19; Ace Glass) under ambient pressure with a total flow of 20 sccm, which carried 3% water vapour so that a 1:1 ratio of CH_4 to H_2O was maintained. The water bubbler was sealed with o-rings and the air tightness was tested regularly. Only pure Milli-Q water was used and the dissolved air was removed by bubbling with He overnight before each experiment. The conversions of CH_4 in all of the experiments (except for the conversion studies) were consistently kept below 5% to minimize mass transfer limitations. Rh-loading-dependent stability was studied for the $Cu_{20-x}Rh_x$ systems, where $x = 0.1, 0.2, 0.5, 1.0$ and 2.0 (Fig. 1b,c). The samples were synthesized using the described method by adjusting the amounts of Cu and Rh precursors. 1.5 mg of the annealed Cu–Rh AR was mounted into the reaction chamber, which was activated by H_2 reduction, as described in the section on catalyst preparation. Samples were illuminated under 0.5 W white light (at a beam diameter of ~1.8 mm and a power density of ~20 W cm^{-2}) without external heating, thus for the photocatalysis studies the only energy source was the light. All samples including the pure Cu and pure Rh were treated under the same conditions, making the results in Fig. 1 comparable to each other. For the wavelength dependence studies (Fig. 2a,b,d), bandpass filters centred at 450, 475, 500, 525, 550, 575, 600, 650 and 700 nm with a width of ±25 nm were used to pick the wavelengths. A constant power of 100 mW (at a beam diameter of ~1.2 mm and a power density of ~8.5 W cm^{-2}) was used for each of the wavelengths by adjusting the neutral-density filter. The reason for using a smaller beam diameter than in the case of the stability tests (Fig. 1) was to obtain a higher power density, since the laser power at some wavelengths was limited after wavelength selection. For blue wavelengths, the supercontinuum laser (Fianium) can only give ~100 mW output (Supplementary Fig. 5b).

Operando measurement of photothermal heating. The surface temperatures of the photocatalysts under illumination were monitored using an infrared camera (A615; FLIR) whose working wavelength range was 7.5–14 μm, precluding interference from the white light laser whose spectrum is shown in Supplementary Fig. 5b. A CaF_2 window was used in the reaction chamber and its external optical transmission coefficient was calibrated to 0.46. Owing to the porous nature of the powder sample, the emissivity of the sample powder was set to 0.95. Details on verification of the accuracy of the infrared camera are provided in our previous publications[39,40,42,53], specifically in supplementary figure 11 of ref. 39, supplementary figure 42 of ref. 40 and supplementary figure 13 of ref. 42. For photocatalysis, the hottest surface temperatures, localized to the laser beam profile, were used to evaluate the photothermal contribution under various illumination conditions. Power dependence studies (Fig. 2e,f) were carried out by changing the illumination power of the white light laser using a neutral-density filter from 150–300 mW, corresponding to power densities from 12.8–25.6 W cm^{-2}. For the partial pressure dependence studies (Fig. 2h and Supplementary Fig. 8c), the CH_4 partial pressure was adjusted between 1.0, 1.5, 3.0, 6.0 and 9.0%, whereas the H_2O partial pressure was kept constant at 3% under 200 mW white light illumination (17 W cm^{-2}). Thermocatalysis of SMR (Fig. 3a–c) was also performed in flow mode under atmospheric pressure. Typically, 5 mg catalyst was loaded into the Harrick reactor. 3% CH_4 and 3% H_2O (balanced by He) were flowed through the catalyst with external heating ranging from 250–550 °C (with a step size of 50 °C) applied to the catalyst without laser illumination. Deactivation and regeneration (Fig. 3d–f) studies included H_2 activation at 500 °C, photocatalysis at 200 mW Fianium illumination, thermocatalysis at 450 °C and photocatalysis at 200 mW, sequentially. After the sequential steps, the sample was transferred to the XPS instrument to study the oxidation states of surface species (Fig. 4a,b). Apparent activation barrier measurements were carried out under constant illumination with externally applied heating. This was the only photocatalytic SMR reaction for which we applied external heating to give temperature gradients for the Arrhenius plots. A monochromatic laser (Chameleon) was used at 467 nm and 300 mW for the studies whose results are shown in Fig. 2g and Supplementary Fig. 8a. Conversion studies (Fig. 2i) were carried out under 3% CH_4 and 3% H_2O, with varying total flow rates under Chameleon illumination (467 nm and 300 mW).

Calibration and quantification of the products

Pure H_2, CO and CO_2 gas cylinders, along with three standard gas cylinders (2.998% H_2, 297.6 ppm H_2, 0.0930% CO and 0.0990% CO_2 balanced with He; AirGas Certified Standard-Spec with an analytical uncertainty of ±2%), were diluted to various known concentrations using the MFCs. The gas mixtures were then fed into the gas chromatograph to obtain the detector response, establishing a calibration curve between the volume (molar) fraction (Δp) and gas chromatography spectrum peak area. For the actual flow-mode catalysis experiment, gas chromatography peak spectra were collected and absolute product rates (r_{abs}) were quantified by total flow rate and the calibration curve, as in equation (1):

$$r_{\mathrm{abs}}\left(\mu\mathrm{mol\,s^{-1}}\right)=\frac{\Delta p\times\mathrm{flow\,(sccm)}}{60\left(\mathrm{s\ min^{-1}}\right)\times 22,400\left(\mathrm{ml\,mol^{-1}}\right)}\times 10^{6}\left(\mu\mathrm{molmol^{-1}}\right) \tag{1}$$

The specific reactivity (r_{Rh}) can be normalized to the mass of Rh (m_{Rh}) present in 1.5 mg catalyst (Fig. 1b) using equation (2):

$$r_{\mathrm{Rh}}\left(\mu\mathrm{mol\,s^{-1}\,mgRh^{-1}}\right)=\frac{r_{\mathrm{abs}}\left(\mu\mathrm{mol\,s^{-1}}\right)}{m_{\mathrm{Rh}}\,(\mathrm{mg})} \tag{2}$$

This is linearly correlated with the TOF using the atomic mass of Rh (102.9 AMU), as in equation (3):

$$\mathrm{TOF}\left(\mathrm{s^{-1}}\right)=r_{\mathrm{Rh}}\left(\mu\mathrm{mol\,s^{-1}\,mgRh^{-1}}\right)\times 102.9\,\mathrm{g\,mol^{-1}} \tag{3}$$

The specific reactivity can also be normalized to the volume of catalyst bed ($V_{\mathrm{catalyst\,bed}}$), resulting in the space–time yield in equation (4):

$$\text{Space-time yield}\left(\mu\mathrm{mol\,cm^{-3}\,s^{-1}}\right)=\frac{r_{\mathrm{abs}}\left(\mu\mathrm{mol\,s^{-1}}\right)}{V_{\mathrm{catalyst\ bed}}\left(\mathrm{cm^{3}}\right)} \tag{4}$$

To compare the reactivity between Cu–Rh and pure Cu, the TOF cannot be used because there are no Rh reactors on pure Cu samples. Thus, the rate is normalized (r_0) to the total mass (m_{catalyst}) of the catalyst in equation (5):

$$r_0\left(\mu\mathrm{mol\,s^{-1}\,g\,catalyst^{-1}}\right)=\frac{r_{\mathrm{abs}}\left(\mu\mathrm{mol\,s^{-1}}\right)}{m_{\mathrm{catalyst}}\,(\mathrm{g})} \tag{5}$$

In the illustrations of catalyst evaluations, H_2 is typically plotted to evaluate the reactivity and stability profile of the catalyst, whereas CO (or CO_2) is expressed as the ratio between CO (or CO_2) and H_2 to account for selectivity.

External quantum efficiencies are plotted in Fig. 2e and defined in equation (6), where N_{A} is the Avogadro constant and E_{photon} is the averaged photon energy, taken as 700 nm for the white light laser.

$$\mathrm{EQE}=\frac{r_{\mathrm{abs}}\left(\mu\mathrm{mol\,s^{-1}}\right)\times N_{\mathrm{A}}\left(\mathrm{mol^{-1}}\right)}{\mathrm{optical\ power}\,(W)/E_{\mathrm{photon}}\,(J)} \tag{6}$$

Error analysis relating to product selectivity was performed using equations (7)–(10):

$$S_{\mathrm{CO}}=\frac{r_{\mathrm{CO}}}{r_{\mathrm{H_2}}} \tag{7}$$

$$\log(S_{\mathrm{CO}})=\log(r_{\mathrm{CO}})-\log(r_{\mathrm{H_2}}) \tag{8}$$

$$\delta[\log(S_{\mathrm{CO}})]=\delta[\log(r_{\mathrm{CO}})]-\delta[\log(r_{\mathrm{H_2}})] \tag{9}$$

$$\frac{\delta S_{\mathrm{CO}}}{S_{\mathrm{CO}}}=\frac{\delta r_{\mathrm{CO}}}{r_{\mathrm{CO}}}-\frac{\delta r_{\mathrm{H_2}}}{r_{\mathrm{H_2}}} \tag{10}$$

According to equation (1), r_{CO} is proportional to Δp (the volume fraction of CO) in the gas mixture. Thus, we have

$$\frac{\delta S_{\mathrm{CO}}}{S_{\mathrm{CO}}}=\frac{\delta V_{\mathrm{CO}}}{V_{\mathrm{CO}}}-\frac{\delta V_{\mathrm{H_2}}}{V_{\mathrm{H_2}}} \tag{11}$$

The standards we use have ±2% analytical uncertainty according to the Certificate of Analysis of Airgas, introducing ±2% error in $\frac{\delta V_{\mathrm{CO}}}{V_{\mathrm{CO}}}$, as well as in $\frac{\delta V_{\mathrm{H_2}}}{V_{\mathrm{H_2}}}$. MFCs used in this experiment contained ±0.6% error according to the technical data of Alicat. All of the above systematic errors could accumulate to $\frac{\delta S_{\mathrm{CO}}}{S_{\mathrm{CO}}}=\pm 2.0\pm 2.0\pm 0.6\pm 0.6=\pm 5.2\%$. The same is true for the CO_2/H_2 ratio measurement.

Study of the electrodynamics of Cu–Rh AR

Monte–Carlo simulations were performed to study the paths of multiple photons within the sample and to evaluate the absorbed photon ratio via a custom-coded program in C. The simulation was based on the Monte–Carlo method outlined previously[58]. The sample was modelled as the mixture of gases (CH_4, H_2O and He) and Cu nanoparticles on $MgO–Al_2O_3$ substrate particles in an 8 × 8 × 5 mm^3 box. The volume fraction of each solid component was estimated based on the total mass of the sample, the molar fraction of each component (based on the synthesis) and the corresponding density. The absorption and scattering coefficients were determined by summing the absorption and scattering cross-sections (σ) weighted by the volume fraction (ρ) of the Cu and substrate particles, as in equations 58 and 59 of ref. 38.

The optical properties of the substrate were calculated for $MgO–Al_2O_3$ particles with sizes ranging from 1–100 μm. The refractive index of the substrate was approximated using the Maxwell–Garnett effective medium model by mixing the dielectric functions of MgO[59] and Al_2O_3[60]. Size distributions of Cu nanoparticles (Supplementary Fig. 3g) were incorporated when calculating the optical cross-section of Cu. The surface effect on the dielectric function was considered using the modified frequency-dependent permittivity, as in equations 47 and 48 of ref. 38. The resulting absorption spectrum is comparable to that of the experimental diffuse reflectance Kubelka–Munk formula (Supplementary Fig. 5a).

The temperature profile of the catalyst pellet was simulated using COMSOL, following the method developed previously[43]. A two-dimensional axisymmetric heat-transfer model in COMSOL Multiphysics 5.6 was used to evaluate the wavelength-dependent temperature of the sample. The system geometry resembled the photocatalysis experimental setup and included three distinct regions: a cylinder-shaped reaction pellet (containing the catalyst and gas) with dimensions of 2 mm diameter and 1 mm height (Supplementary Fig. 5c); a steel cylinder ring (supporting the reaction pellet) with an inner radius of 1 mm, an outer radius of 3.1 mm and a height of 2.5 mm; and a steel cylinder box with a diameter of 10 mm and a height of 20 mm, which contained the pellet and steel ring and was filled with environmental gas at a pressure of 1 atm.

When illuminated with normal incidence light, the reaction pellet absorbed a fraction of the laser power, which was then converted to heat. The light intensity decreased exponentially along the incident direction, resulting in a penetration depth of ~10 μm[41]. Two-dimensional surface heating was applied to the top surface of the reaction pellet to model the heat source, which followed a Gaussian distribution based on the quasi-Gaussian beam profile of the incident laser (supplementary figure 4 of ref. 38). The magnitude of the heat source was the product of the incident laser power and the wavelength-dependent absorbance of the sample, which was obtained from the Monte–Carlo simulation (Supplementary Fig. 5a). When white light was used, the spectrum of the white light laser (Supplementary Fig. 5b) was also included as a weight factor.

The thermal conductivity of the solid–gas mixture in the sample pellet and solid $Cu–MgO–Al_2O_3$ was calculated using the Maxwell–Garnett effective medium model. The gas in the mixture was the same as in the photocatalysis experiment (CH_4, H_2O and He). The temperature-dependent thermal conductivity of the gas mixture was calculated using the Wassiljewa equation with the Lindsay and Bromley coefficient[61].

$$k_{\mathrm{mix}}=\sum_{i=1}^{n}\frac{x_i k_i}{\sum_{j=1}^{n}A_{ij}x_j} \tag{12}$$

$$A_{ij} = \frac{1}{4}\left\{1 + \left[\frac{\mu_i}{\mu_j}\left(\frac{M_j}{M_i}\right)^{\frac{3}{4}} \frac{1+\frac{S_i}{T}}{1+\frac{S_j}{T}}\right]^{\frac{1}{2}}\right\}^2 \frac{1+\frac{S_{ij}}{T}}{1+\frac{S_j}{T}} \tag{13}$$

where x_i, k_i, μ_i, M_i and S_i are the mole fraction, thermal conductivity, dynamic viscosity, molecular weight and Sutherland constant of the i-th gas, respectively. Values of the temperature-dependent thermal conductivity of the pure gas were obtained from ref. 62. Values of the temperature-dependent dynamic viscosity were obtained from ref. 63. Values of Sutherland's constant were from ref. 64. The resulting photothermal heating spectrum predicted the general trend of the experimental results (Supplementary Fig. 5d).

Hot carrier injection rate simulation

A hot carrier injection model (Fig. 2c, inset) was used to simulate the wavelength-dependent reactivity (Fig. 2a) following the method of a previous study (equations 50–56 in ref. 38), which modelled the generation and injection of hot carriers in plasmonic photocatalysis. Three sources of hot carrier generation were included to calculate the hot carrier distribution: direct interband transitions; intraband transitions due to Drude damping; and geometry-assisted intraband transitions (Landau damping). The ratio of each component was determined from the corresponding imaginary part of the permittivity. The initial carrier distribution from a direct interband transition was dependent on the electronic structure and was evaluated using the quantum mechanics software JDFTx[51,65]. The Drude electron and geometry-assisted hot electron generation rate could be approximated using classical calculations. The hot carrier injection rate spectrum was determined by integrating the product of the density of states of the adsorbate antibonding orbital and the rate of overall hot carrier generation over the carrier energy (equation 56 in ref. 38). The antibonding orbital was approximated as a Lorentzian function with a centre energy ε_0 and a line width of 0.1 eV. The normalized spectra of hot carrier injections for various ε_0 values are plotted in Fig. 2c.

Data availability

Additional datasets generated and/or analysed during the current study that are not included in the published Article and associated Supplementary Information, including the atomic coordinates for the JDFTx calculations, are available from the open-access Zenodo repository at https://doi.org/10.5281/zenodo.13377300 (ref. 66).

Code availability

Python codes for the EM simulation and hot carrier distribution calculations are available from the open-access Zenodo repository at https://doi.org/10.5281/zenodo.13377300 (ref. 66).

References

1. Guo, X. et al. Direct, nonoxidative conversion of methane to ethylene, aromatics, and hydrogen. *Science* **344**, 616–619 (2014).
2. Upham, D. C. et al. Catalytic molten metals for the direct conversion of methane to hydrogen and separable carbon. *Science* **358**, 917–921 (2017).
3. Sushkevich, V. L., Palagin, D., Ranocchiari, M. & Van Bokhoven, J. A. Selective anaerobic oxidation of methane enables direct synthesis of methanol. *Science* **356**, 523–527 (2017).
4. Jin, Z. et al. Hydrophobic zeolite modification for in situ peroxide formation in methane oxidation to methanol. *Science* **367**, 193–197 (2020).
5. Li, X., Xie, J., Rao, H., Wang, C. & Tang, J. Platinum- and CuO_x-decorated TiO_2 photocatalyst for oxidative coupling of methane to C_2 hydrocarbons in a flow reactor. *Angew. Chem. Int. Ed.* **59**, 19702–19707 (2020).
6. Yu, X. et al. Stoichiometric methane conversion to ethane using photochemical looping at ambient temperature. *Nat. Energy* **5**, 511–519 (2020).
7. Morejudo, S. H. et al. Direct conversion of methane to aromatics in a catalytic co-ionic membrane reactor. *Science* **353**, 563–566 (2016).
8. Hu, A., Guo, J.-J., Pan, H. & Zuo, Z. Selective functionalization of methane, ethane, and higher alkanes by cerium photocatalysis. *Science* **361**, 668–672 (2018).
9. Nikolaidis, P. & Poullikkas, A. A comparative overview of hydrogen production processes. *Renew. Sustain. Energy Rev.* **67**, 597–611 (2017).
10. Kannah, R. Y. et al. Techno-economic assessment of various hydrogen production methods—a review. *Bioresour. Technol.* **319**, 124175 (2021).
11. Schulz, H. Short history and present trends of Fischer–Tropsch synthesis. *Appl. Catal. A* **186**, 3–12 (1999).
12. Dry, M. E. The Fischer–Tropsch process: 1950–2000. *Catal. Today* **71**, 227–241 (2002).
13. Jiao, F. et al. Disentangling the activity–selectivity trade-off in catalytic conversion of syngas to light olefins. *Science* **380**, 727–730 (2023).
14. Van Hook, J. P. Methane–steam reforming. *Catal. Rev.* **21**, 1–51 (1980).
15. Meng, X. et al. Direct methane conversion under mild condition by thermo-, electro-, or photocatalysis. *Chem* **5**, 2296–2325 (2019).
16. Li, Q., Ouyang, Y., Li, H., Wang, L. & Zeng, J. Photocatalytic conversion of methane: recent advancements and prospects. *Angew. Chem. Int. Ed.* **61**, e202108069 (2022).
17. Li, X., Wang, C. & Tang, J. Methane transformation by photocatalysis. *Nat. Rev. Mater.* **7**, 617–632 (2022).
18. Yoshida, H., Kato, S., Hirao, K., Nishimoto, J.-I. & Hattori, T. Photocatalytic steam reforming of methane over platinum-loaded semiconductors for hydrogen production. *Chem. Lett.* **36**, 430–431 (2007).
19. Shimura, K. et al. Photocatalytic steam reforming of methane over sodium tantalate. *J. Phys. Chem. C* **114**, 3493–3503 (2010).
20. Shimura, K., Kawai, H., Yoshida, T. & Yoshida, H. Bifunctional rhodium cocatalysts for photocatalytic steam reforming of methane over alkaline titanate. *ACS Catal.* **2**, 2126–2134 (2012).
21. Yamamoto, A., Mizuba, S., Saeki, Y. & Yoshida, H. Platinum loaded sodium tantalate photocatalysts prepared by a flux method for photocatalytic steam reforming of methane. *Appl. Catal. A* **521**, 125–132 (2016).
22. Song, H. et al. Visible-light-mediated methane activation for steam methane reforming under mild conditions: a case study of Rh/TiO_2 catalysts. *ACS Catal.* **8**, 7556–7565 (2018).
23. Han, B., Wei, W., Li, M., Sun, K. & Hu, Y. H. A thermo-photo hybrid process for steam reforming of methane: highly efficient visible light photocatalysis. *Chem. Commun.* **55**, 7816–7819 (2019).
24. Linic, S., Christopher, P. & Ingram, D. B. Plasmonic-metal nanostructures for efficient conversion of solar to chemical energy. *Nat. Mater.* **10**, 911–921 (2011).
25. Brongersma, M. L., Halas, N. J. & Nordlander, P. Plasmon-induced hot carrier science and technology. *Nat. Nanotechnol.* **10**, 25–34 (2015).
26. Aslam, U., Chavez, S. & Linic, S. Controlling energy flow in multimetallic nanostructures for plasmonic catalysis. *Nat. Nanotechnol.* **12**, 1000–1005 (2017).
27. Robatjazi, H., Yuan, L., Yuan, Y. & Halas, N. J. in *Emerging Trends in Chemical Applications of Lasers* Vol. 1398, 363–387 (ACS Symposium Series, American Chemical Society, 2021).
28. Mukherjee, S. et al. Hot-electron-induced dissociation of H_2 on gold nanoparticles supported on SiO_2. *J. Am. Chem. Soc.* **136**, 64–67 (2013).

29. Lou, M. et al. Direct H_2S decomposition by plasmonic photocatalysis: efficient remediation plus sustainable hydrogen production. *ACS Energy Lett.* **7**, 3666–3674 (2022).
30. Contreras, E. et al. Plasmon-assisted ammonia electrosynthesis. *J. Am. Chem. Soc.* **144**, 10743–10751 (2022).
31. Christopher, P., Xin, H. & Linic, S. Visible-light-enhanced catalytic oxidation reactions on plasmonic silver nanostructures. *Nat. Chem.* **3**, 467–472 (2011).
32. Devasia, D., Wilson, A. J., Heo, J., Mohan, V. & Jain, P. K. A rich catalog of C–C bonded species formed in CO_2 reduction on a plasmonic photocatalyst. *Nat. Commun.* **12**, 2612 (2021).
33. Marimuthu, A., Zhang, J. & Linic, S. Tuning selectivity in propylene epoxidation by plasmon mediated photo-switching of Cu oxidation state. *Science* **339**, 1590–1593 (2013).
34. Zhou, L. et al. Aluminum nanocrystals as a plasmonic photocatalyst for hydrogen dissociation. *Nano Lett.* **16**, 1478–1484 (2016).
35. Swearer, D. F. et al. Heterometallic antenna–reactor complexes for photocatalysis. *Proc. Natl Acad. Sci. USA* **113**, 8916–8920 (2016).
36. Sytwu, K. et al. Driving energetically unfavorable dehydrogenation dynamics with plasmonics. *Science* **371**, 280–283 (2021).
37. Halas, N. J. et al. Multicomponent plasmonic photocatalysts consisting of a plasmonic antenna and a reactive catalytic surface: the antenna–reactor effect. US patent US10766024B2 (2020).
38. Yuan, Y. et al. Earth-abundant photocatalyst for H_2 generation from NH_3 with light-emitting diode illumination. *Science* **378**, 889–893 (2022).
39. Zhou, L. et al. Quantifying hot carrier and thermal contributions in plasmonic photocatalysis. *Science* **362**, 69–72 (2018).
40. Zhou, L. et al. Light-driven methane dry reforming with single atomic site antenna–reactor plasmonic photocatalysts. *Nat. Energy* **5**, 61–70 (2020).
41. Robatjazi, H. et al. Plasmon-induced selective carbon dioxide conversion on Earth-abundant aluminum–cuprous oxide antenna–reactor nanoparticles. *Nat. Commun.* **8**, 27 (2017).
42. Robatjazi, H. et al. Plasmon-driven carbon–fluorine ($C(sp^3)$–F)) bond activation with mechanistic insights into hot-carrier-mediated pathways. *Nat. Catal.* **3**, 564–573 (2020).
43. Zhou, L. et al. Hot carrier multiplication in plasmonic photocatalysis. *Proc. Natl Acad. Sci. USA* **118**, e2022109118 (2021).
44. Jones, G. et al. First principles calculations and experimental insight into methane steam reforming over transition metal catalysts. *J. Catal.* **259**, 147–160 (2008).
45. Besenbacher, F. et al. Design of a surface alloy catalyst for steam reforming. *Science* **279**, 1913–1915 (1998).
46. Marcinkowski, M. D. et al. Pt/Cu single-atom alloys as coke-resistant catalysts for efficient C–H activation. *Nat. Chem.* **10**, 325–332 (2018).
47. Hannagan, R. T. et al. First-principles design of a single-atom-alloy propane dehydrogenation catalyst. *Science* **372**, 1444–1447 (2021).
48. Behrens, M. et al. The active site of methanol synthesis over Cu/ZnO/Al_2O_3 industrial catalysts. *Science* **336**, 893–897 (2012).
49. Behrens, M. Coprecipitation: an excellent tool for the synthesis of supported metal catalysts—from the understanding of the well known recipes to new materials. *Catal. Today* **246**, 46–54 (2015).
50. Boudart, M. Turnover rates in heterogeneous catalysis. *Chem. Rev.* **95**, 661–666 (1995).
51. Brown, A. M., Sundararaman, R., Narang, P., Goddard, W. A. & Atwater, H. A. Nonradiative plasmon decay and hot carrier dynamics: effects of phonons, surfaces, and geometry. *ACS Nano* **10**, 957–966 (2016).
52. Zhou, L. et al. Response to comment on "Quantifying hot carrier and thermal contributions in plasmonic photocatalysis". *Science* **364**, eaaw9545 (2019).
53. Robatjazi, H. et al. Reply to: Distinguishing thermal from non-thermal contributions to plasmonic hydrodefluorination. *Nat. Catal.* **5**, 247–250 (2022).
54. Mukherjee, S. et al. Hot electrons do the impossible: plasmon-induced dissociation of H_2 on Au. *Nano Lett.* **13**, 240–247 (2013).
55. Linic, S., Aslam, U., Boerigter, C. & Morabito, M. Photochemical transformations on plasmonic metal nanoparticles. *Nat. Mater.* **14**, 567–576 (2015).
56. Lindstrom, C. D. & Zhu, X. Y. Photoinduced electron transfer at molecule–metal interfaces. *Chem. Rev.* **106**, 4281–4300 (2006).
57. Kim, K. H., Watanabe, K., Mulugeta, D., Freund, H.-J. & Menzel, D. Enhanced photoinduced desorption from metal nanoparticles by photoexcitation of confined hot electrons using femtosecond laser pulses. *Phys. Rev. Lett.* **107**, 047401 (2011).
58. Seemala, B. et al. Plasmon-mediated catalytic O_2 dissociation on Ag nanostructures: hot electrons or near fields? *ACS Energy Lett.* **4**, 1803–1809 (2019).
59. Stephens, R. E. & Malitson, I. H. Index of refraction of magnesium oxide. *J. Res. Nat. Bur. Stand.* **49**, 249–252 (1952).
60. Edward, D. P. *Handbook of Optical Constants of Solids* (Academic Press, 1998).
61. Lindsay, A. L. & Bromley, L. A. Thermal conductivity of gas mixtures. *Ind. Eng. Chem.* **42**, 1508–1511 (1950).
62. Touloukian, Y. S., Liley, P. E. & Saxena, S. C. *Thermophysical Properties of Matter—the TPRC Data Series* Vol. 3 (IFI/Plenum, 1970).
63. Touloukian, Y. S., Saxena, S. C. & Hestermans, P. *Thermophysical Properties of Matter—the TPRC Data Series* Vol. 11 (IFI/Plenum, 1975).
64. Crane, C. *Flow of Fluids Through Valves, Fittings, and Pipe* (Crane Company, 1988).
65. Sundararaman, R. et al. JDFTx: software for joint density-functional theory. *SoftwareX* **6**, 278–284 (2017).
66. Yuan, Y. et al. Steam methane reforming using a regenerable antenna-reactor plasmonic photocatalyst. *Zenodo* https://doi.org/10.5281/zenodo.13377300 (2024).

Acknowledgements

This article is based on work supported by the Robert A. Welch Foundation under grants C-1220 (to N.J.H.) and C-1222 (to P.N.) and by the Air Force Office of Scientific Research via the Department of Defense Multidisciplinary University Research Initiative under AFOSR Award number FA9550-15-1-0022. We acknowledge B. Chen from the Shared Equipment Authority at Rice University for providing valuable insights and assistance with processing the XPS data.

Author contributions

Y.Y., P.N. and N.J.H. initiated the project. Y.Y. developed the photocatalyst, performed the characterization, studied the catalysis and analysed the data. J.Z. performed the theoretical simulations. A.B. performed the scanning transmission electron microscopy. H.R. helped to interpret the data. P.N. and N.J.H. supervised the research. All authors contributed to preparation of the manuscript.

Competing interests

The antenna–reactor concept is protected under US patents US10766024B2 and US11958043B2, with additional coverage pending in published US patent application US20210023541A1. The antenna–reactor concept is also described in the international patent application WO 2018/231398 A2. Syzygy Plasmonics owns several patents relating to the photoreactor platform. N.J.H. and P.N. are co-founders of Syzygy Plasmonics. N.J.H., P.N. and H.R. have interest in Syzygy Plasmonics and hold equity in the company. The remaining authors declare no competing interests.

Additional information

Supplementary information The online version contains supplementary material available at https://doi.org/10.1038/s41929-024-01248-8.

Correspondence and requests for materials should be addressed to Peter Nordlander or Naomi J. Halas.

Peer review information *Nature Catalysis* thanks Jennifer Dionne, Hisao Yoshida and the other, anonymous, reviewer(s) for their contribution to the peer review of this work.

Reprints and permissions information is available at www.nature.com/reprints.

Publisher’s note Springer Nature remains neutral with regard to jurisdictional claims in published maps and institutional affiliations.

Springer Nature or its licensor (e.g. a society or other partner) holds exclusive rights to this article under a publishing agreement with the author(s) or other rightsholder(s); author self-archiving of the accepted manuscript version of this article is solely governed by the terms of such publishing agreement and applicable law.

© The Author(s), under exclusive licence to Springer Nature Limited 2024